Supporting Information

2D surface induced self-assemble of Pd nanocrystals into nanostrings for enhanced formic acid electroxidation

Sheng Zhang*[,1], Rong Xia[1], Yaqiong Su[6,*], Yichao Zou[5], Chengyi Hu[4], Geping Yin[3], Emiel, J.M. Hensen[6], Xinbin Ma[1], Yuehe Li[2,*]

[1] Key Laboratory for Green Chemical Technology of Ministry of Education, Collaborative Innovation Centre of Chemical Science and Engineering, School

of Chemical Engineering and Technology, Tianjin University, Tianjin 300072, China. E-mail: sheng.zhang@tju.edu.cn (ORCID: 0000-0001-7532-1923)

[2] School of Mechanical and Materials Engineering, Washington State University, WA 99164, USA. Email: yuehe.lin@wsu.edu (ORCID: 0000-0003-3791-7587)

[3] State Key Laboratory of Urban Water Resource and Environment, School of Chemistry and Chemical Engineering, Harbin Institute of Technology, Harbin 150001, China.

[4] College of Chemistry and Chemical Engineering, iChEM, Xiamen University, Xiamen 361005, China.

[5] School of Materials, University of Manchester, UK, M13 9PL.

[6] Laboratory of Inorganic Materials and Catalysis, Department of Chemical Engineering and Chemistry, Eindhoven University of Technology, P.O. Box

513, 5600 MB Eindhoven, The Netherlands. E-mail: Y-Q.Su@tue.nl

Section 1: Experimental details

Experimental Section

Synthesis of graphite oxide[1]

Graphite oxide (GO) was prepared with the modified Hummers method. Typically, 5.0 g graphite powder (<45 μm, Sigma-Aldrich) was added into 180 mL concentrated H_2SO_4 and stirred for 1 h in a hood. Then 60 mL fuming HNO_3 was slowly added to the mixture under ice-cooling and stirring. After cooling down, 25 g $KMnO_4$ was slowly added under ice-cooling and stirring. The mixed slurry was stirred at room temperature in a hood for 120 h. After that, 600 mL deionized (DI) water was slowly added into the reacted slurry and stirred for 2 h; then 30 mL H_2O_2 (30%) was added, and the slurry immediately turned into a bright yellow solution with bubbling. The resultant solution was stirred for 2 h and then allowed to settle down for 24 h; after that, the supernatant was decanted. The resultant yellow slurry was centrifuged and then washed in 1000 mL DI water with 5 mL HCl (37%) and 3 mL H_2O_2 (30%) added. After stirring for 2 h, the solution was centrifuged and then washed again. This process was repeated three times. After that, the yellow slurry was further washed with 500 mL DI water until the pH of the washing solution increased to neutral (6.5) (it took about 500 mL × 12 washes). The remaining dark-yellow solid was dried under vacuum at 40°C for 48 h and ground to a fine powder. The dry process for GO must be carried out at low temperatures because it slowly decomposes (deoxygenates) above 60 to 80 °C.

Synthesis of Pd nanoparticles (Pd NPs)[2,3]

Pd NPs were synthesized using a colloidal method. In brief, a 2.3 mL K_2PdCl_4 (30.6 mM) solution was added into 200 mL DI water containing 300 μl 35 wt. % PDDA (average MW < 100 000) under stirring for 10 min. Then freshly prepared $NaBH_4$ solution (20 mg $NaBH_4$ in 5 mL H_2O) was injected, where the color of solution immediately changed to dark. After reaction for 5 min, highly dispersed Pd NPs with 2~3 nm in diameter were obtained.

Synthesis of Pd nanostrings /graphene (Pd NS/G)

30 mg GO powder was added into 20 mL DI water and then ultrasonicated for 10 min to obtain exfoliated GO solution. Then the as-prepared Pd NPs (7.5 mg Pd) suspensions were mixed with the above GO solution, and stirred for 10 min. Then 500 mg $NaBH_4$ was added, and then the solution color changed from yellow-brown to black, indicating the reduction of GO to graphene nanosheets. After an additional 24 h of stirring, the resultant Pd NS/G was filtered and washed with DI water until no Cl^- was detected and then dried in vacuum at 90 °C for 3 h. In this case, Pd NPs reorganized into Pd NS network on the surface of graphene (Fig. 1C-D, Fig. S3). For comparison, we also mixed pre-reduced GO solution (using the same amount of $NaBH_4$ for the same GO solution; the reaction solution ($NaBH_4$+GO+DI water) was not washed, i.e., the electrolyte ($NaBH_4 \rightarrow NaBO_2$) still remained in the solution, therefore, the only difference is the sequence of $NaBH_4$ addition) with Pd NPs solution. In this case, Pd NPs did not reorganize into Pd NS network (Fig. 2B, Fig. S6).

In addition, we also replaced GO with carbon black (Vulcan carbon XC-72) and carbon nanotubes (Cheaptubes, USA) and mixed them with Pd NPs solution followed by the addition of $NaBH_4$ (the same as that for GO) (Fig. S8).

Synthesis of Pd NPs/G, Pd NPs/XC-72, Pd NPs/CNT[2,3]

For preparation of Pd NPs/G, first, 30 mg GO powder was added into 20 mL H_2O to obtain exfoliated GO solution by ultrasonication. Then 500 mg $NaBH_4$ was introduced to reduce the GO. The solution was filtrated, washed, dried in vacuum at room temperature to obtain chemically reduced graphene oxide powder. The obtained graphene powder was mixed with the as-prepared Pd NPs-PDDA suspension under vigorous stirring. After an additional 48 h of stirring, the resultant Pd NPs/G was filtered and washed with DI water until no Cl^- was detected and then dried in vacuum at 90 °C for 3 h. The preparation of Pd NPs/XC-72 was similar to Pd NPs/G by mixing XC-72 carbon black and as-prepared Pd NPs-PDDA solution followed by filtration, washing and dry in the same way as in the case Pd NPs/G. Pd NPs/G (Fig. S7) and Pd NPs/C (Fig. S9).

Materials characterization

Transmission electron microscopy (TEM) images of the catalysts were taken on a JEOL TEM 2010 microscope equipped with an Oxford ISIS system. The operating voltage on the microscope was 200 keV. All images were digitally recorded with a slow-scan charged-coupled device (CCD) camera. X-ray diffraction (XRD) patterns were obtained using a Philips Xpert X-ray diffractometer using Cu Kα radiation at λ= 1.54 Å. X-ray photoelectron spectroscopy (XPS) measurements were performed using a Physical Electronics Quantum 2000 Scanning ESCA Microprobe. This system uses a focused monochromatic Al Kα x-rays (1486.7 eV) source and a spherical section analyzer. The instrument has a 16 element multichannel detector. The X-ray beam used was a 100 W, 100 mm diameter beam that was rastered over a 1.3 mm by 0.2 mm rectangle on the sample. The X-ray beam is incident normal to the sample and the photoelectron detector was at 45° off-normal using an analyzer angular acceptance width of 20° x 20°. Wide scan data was collected using a pass energy of 117.4 eV. For the Ag3d5/2 line, these conditions produce FWHM of better than 1.6 eV. High energy resolution spectra was collected using a pass energy of 46.95 eV. For the Ag3d5/2 line, these conditions produced FWHM of better than 0.98 eV. The binding energy (BE) scale is calibrated using the $Cu2p_{3/2}$ feature at 932.62 ± 0.05 eV and Au 4f at 83.96 ± 0.05 eV for known standards.

Electrochemical measurements

Electrochemical tests were carried out in a standard three-electrode system controlled with a CHI660C station (CH Instruments, Inc., USA) with Pt wire and Hg/Hg_2SO_4 as the counter electrode and reference electrode, respectively. All the electrode potentials are scaled to reversible hydrogen electrode (RHE). The working electrodes were prepared by applying catalyst ink onto the pre-polished glass carbon disk electrodes. In brief, the electrocatalyst was dispersed in ethanol and ultrasonicated for 15 minutes to form a uniform catalyst ink (2 mg mL 1). A total of 7.5 µL of well- dispersed catalyst ink was applied onto the pre-polished glassy carbon (GC) disk electrode (5 mm in diameter). After drying at room temperature, 2×5 µL 0.05 wt% Nafion solution was applied onto the surface of the catalyst layer to form a thin protective film. The well-prepared electrodes were dried at room temperature overnight before electrochemical tests. The samples are uniformly dispersed on glass carbon disk electrodes. The total loading of the catalyst was 15 µg (3 µg Pd). Working electrodes were first activated with cyclic voltammograms (CVs) (0 to 1.0 V at 50 mV s^{-1}) in N_2-purged 0.5 M H_2SO_4 solution until a steady CV was obtained. To measure formic acid electroxidation, the solution of 0.5 M H_2SO_4 + 0.5 M HCOOH was purged with N_2 gas before measurements were taken, and CVs were recorded at the scan rate of 50 mV s^{-1}. The amperometric current density-time (*i-t*) curves were

measured at a fixed potential of 0.3 V for 1 h. Accelerated durability tests (ADT) were performed on the working electrode by cycling the voltage between 0 V and 0.9 V in a N_2-purged 0.5 M H_2SO_4 solution at the scan rate of 50 mV s^{-1} for 500 CV cycles. All the tests were conducted at room temperature. All potentials were reported versus the reversible hydrogen electrode (RHE).

Section 2: Materials Characterization

Fig. S1 Digital photos of the exfoliated GO aqueous solution with Pd NPs (A) and without Pd NPs (B) recorded at 0 min, 1 min, and 60 min after the addition of $NaBH_4$.

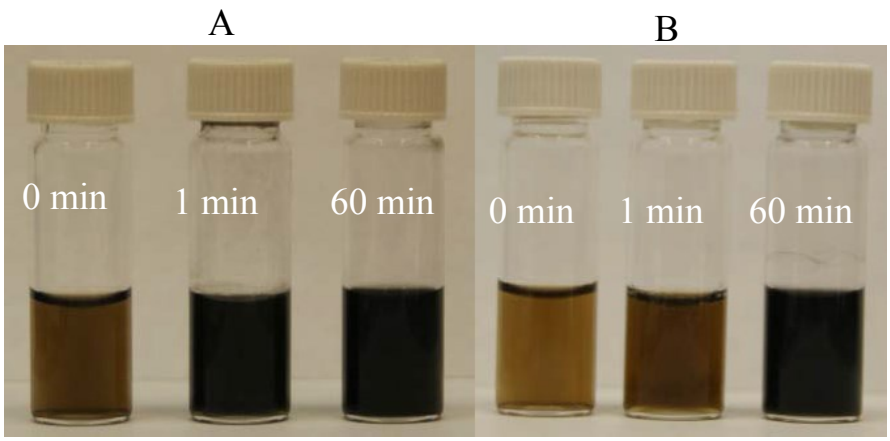

Fig. S2 TEM images of as-prepared Pd NPs synthesized in PDDA aqueous solution.

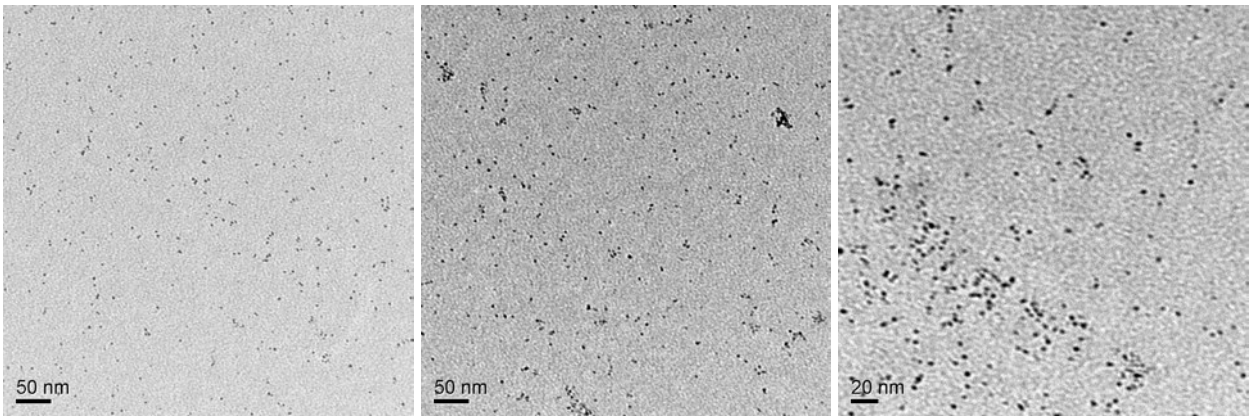

Fig. S3 TEM images of Pd nanotrings/G (PdNP-PDDA solution mixed with GO solution and then reduced with $NaBH_4$).

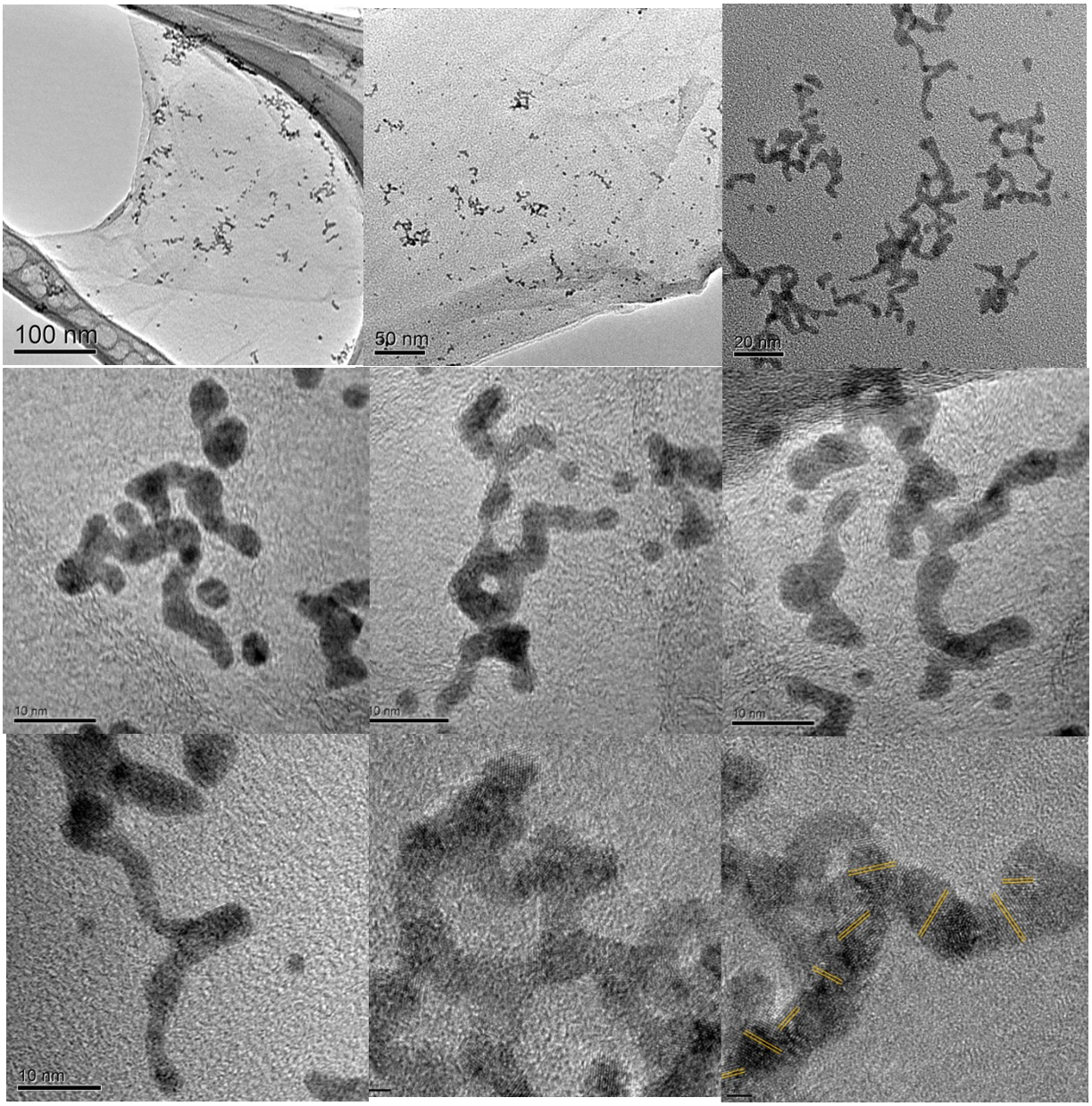

Fig. S4 TEM images of Pd NPs on graphene oxide (PdNP-PDDA solution mixed with GO solution).

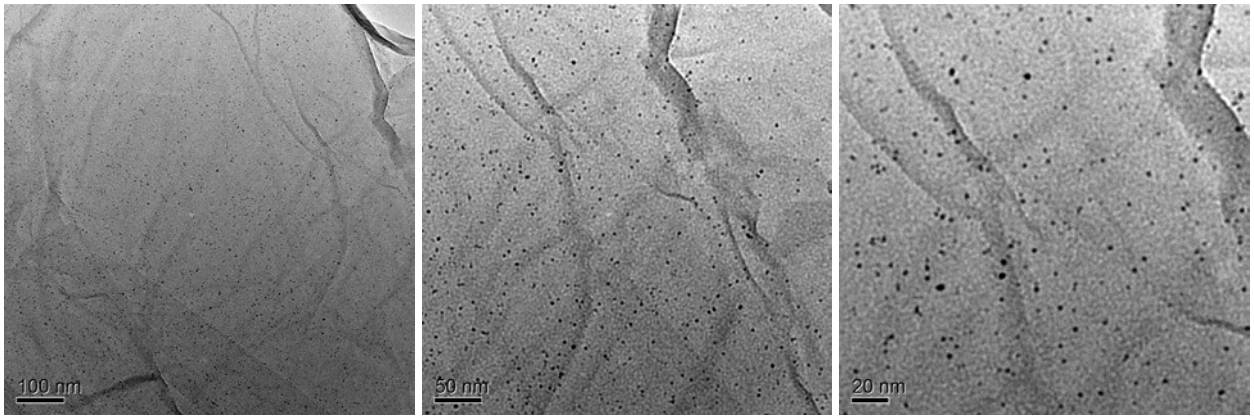

Fig. S5 TEM images of (a) Pd NPs on GO (pH=12.5) and (b) Pd NPs on pre-reduced graphene oxide (mixing $NaBH_4$-reduced GO solution and Pd NPs solution).

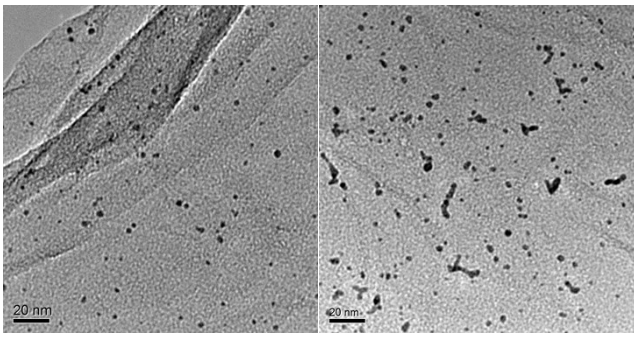

Fig. S6 TEM images of Pd NPs on GO at pH=12.5 (Pd NP-PDDA solution mixed with GO solution, and then the pH values were modified with NaOH to 12.5).

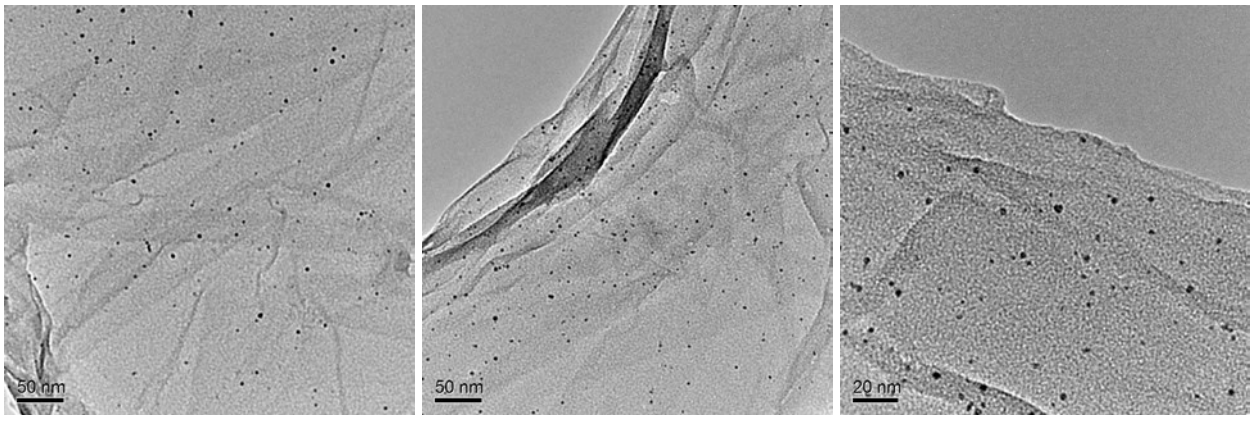

Fig. S7 TEM images of Pd NPs on pre-reduced GO (PdNP-PDDA solution mixed with $NaBH_4$-reduced GO solution; the electrolyte ($NaBH_4 \rightarrow NaBO_2$) after GO reduction was not removed from the solution.)

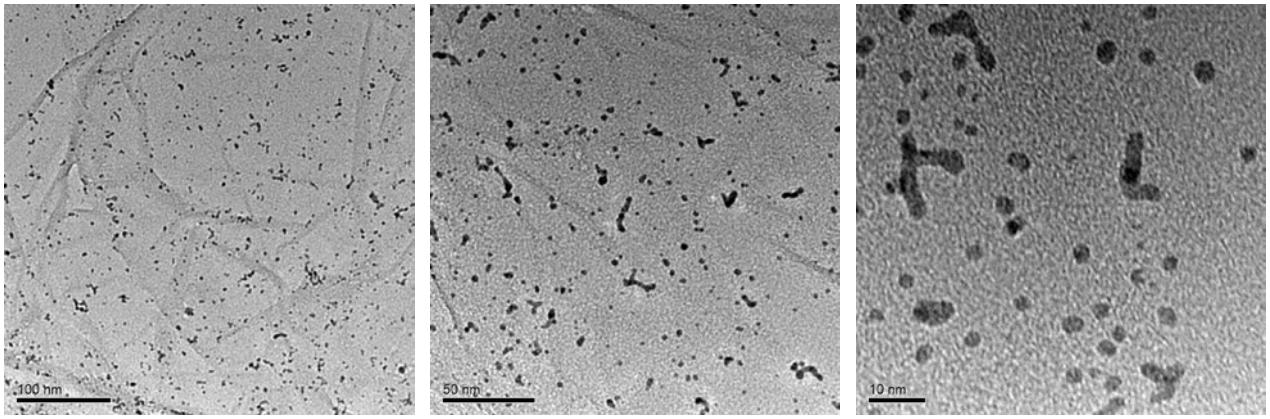

Fig. S8 TEM images of Pd NPs on pre-reduced GO powder (GO was first reduced with $NaBH_4$ and then washed to obtain chemically reduced GO powder; then PdNP-PDDA solution was mixed with $NaBH_4$-reduced GO powder).

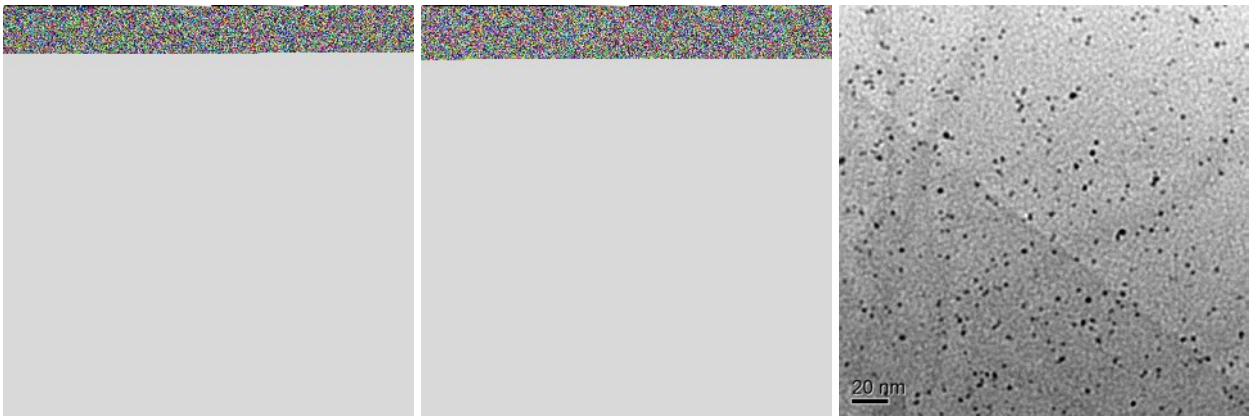

Fig. S9 TEM images of Pd NPs-PDDA/XC-72 and Pd NPs-PDDA/CNT

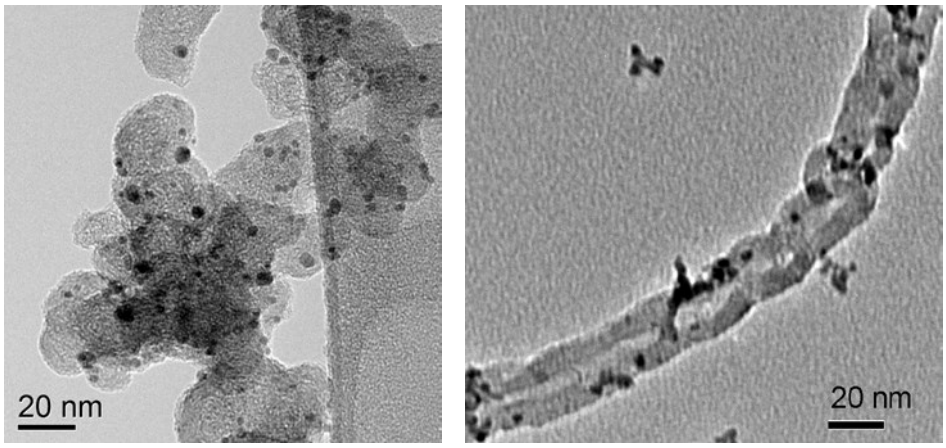

Fig. S10 TEM image of Pd NPs/C.

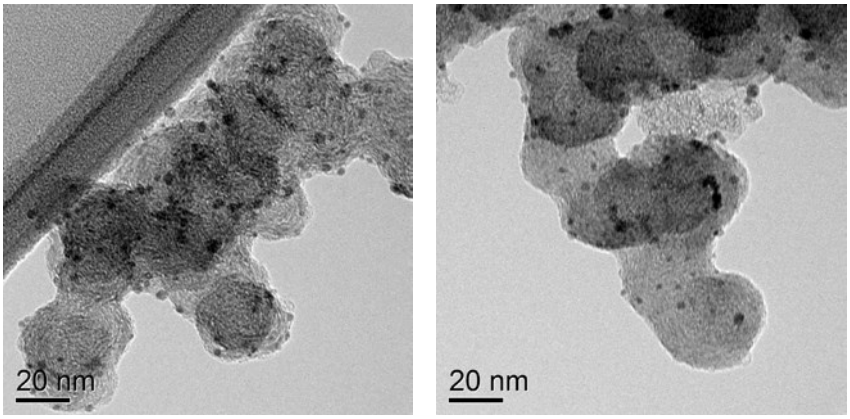

Section 3: Electrochemical tests

Fig. S11 Cyclic voltammograms (50 mV s^{-1}) of Pd NS/G and PdNPs/G in N_2-saturated 0.5 M H_2SO_4.

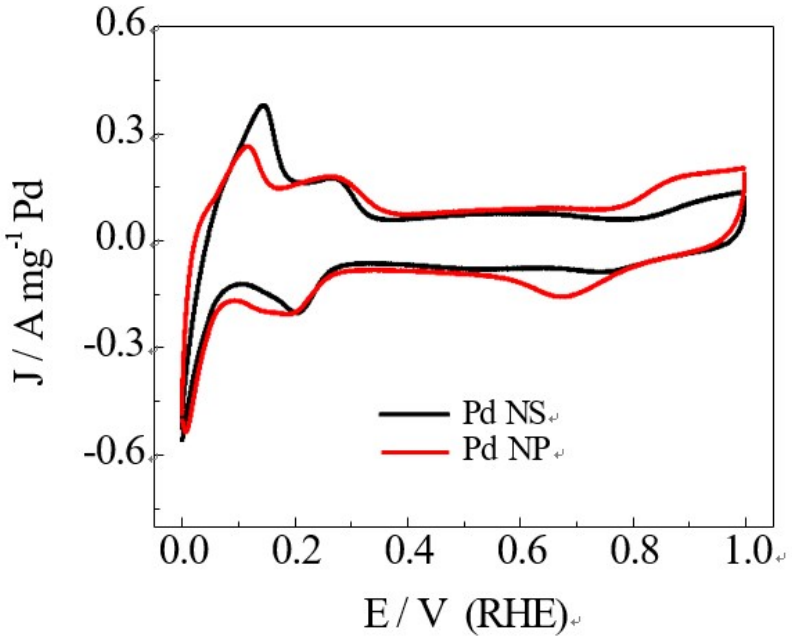

Fig. S11 shows cyclic voltammograms (50 mV s^{-1}) of Pd NS/G and Pd NP/G in N_2-saturated 0.5 M H_2SO_4. It has been reported that the different morphology (shape and size) of metal nanoparticles will lead to different d-band center energy,[4,5] which plays a key role in the adsorption behavior of species (especially for O/OH).[6,7] This can be seen from in CVs the different oxygen adsorption/desorption behavior. The oxygen (O/OH) adsorption on Pd NS/G is significantly suppressed (the fractional coverage by (O/OH)ad (Q(O/OH)ad) on Pd NS network is dramatically reduced by 57% relative to Pd NPs/G) and its onset potential is positively shifted by ~50mV in comparison with Pd NPs/G.

The adsorbed O/OH is considered to be the contributor to the deactivation of Pd activity for HCOOH oxidation.[8,9] Therefore, the higher electrocatalytic activity towards HCOOH on Pd NS/graphene probably results from the appropriate d-band center energy of Pd NS,[4,5] which weakens the interaction between the Pd surface atoms and nonreactive oxygenated species (OH) and increases the number of Pd active sites for HCOOH oxidation.

Generally, the degradation in the electrochemical surface area (ESA) of nanoscale Pd particles mainly results from the following reasons: the dissolution, Ostwald ripening and aggregation of Pd. As shown in Fig. S11, above 0.75 V, the surface reaction involves the formation of PdOH and PdO derived from the oxidation of water that causes the dissolution of Pd via the

Pd^{2+} oxidation state.[10] The positively-shifted onset potential of O/OH formation on Pd NS/G and the suppressed O/OH adsorption indicates the higher oxidation resistance of Pd NS than Pd NPs. This may be attributed to the different electronic structure of surface Pd atoms in these two samples,[7,10] which leads to higher stability of metal nanoparticles.[10] In addition, large aspect ratio of Pd NW will prevent Pd from Ostwald ripening and aggregating on graphene nanosheets.[11,12]

Fig. S12 The *i-t* curves (0.3 V vs. RHE) of HCOOH oxidation (0.5M H_2SO_4+0.5 M HCOOH) at Pd NS/G, Pd NPs/G, Pd NPs/carbon black (before accelerated degradation test).

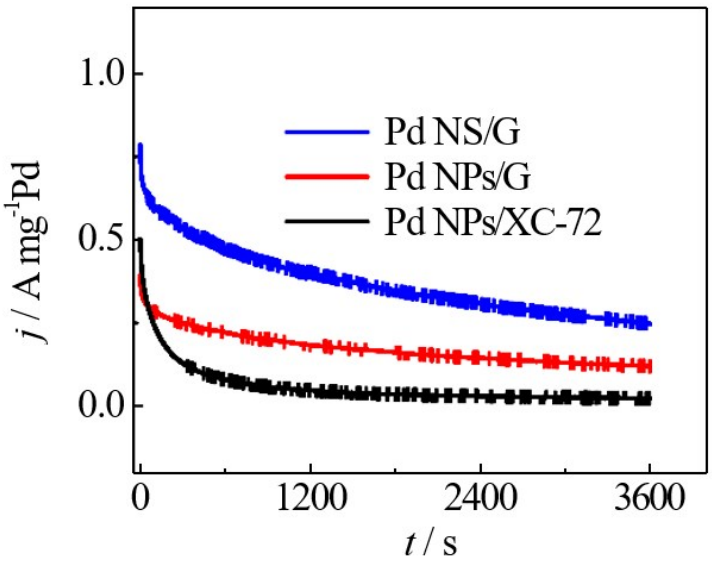

The mass activity (0.25 A mg^{-1} Pd at 0.3 V vs. RHE) of our Pd NS/G is much higher than previously reported Pd-based electrocatalysts: Pd NS without a support (~0.1 A mg^{-1} Pd at 0.1 V Ag/AgCl, the potential of Ag/AgCl is about 0.2 V vs RHE),[13] PdNP/carbon black (0.165 A mg^{-1} Pd at 0.2 V Ag/AgCl) [14] and PdNP/carbon nanotubes (~ 0.060 A mg^{-1} Pd)[15-17]. It is also higher than alloy electrocatalyts, such as PtBi (0.22 A mg^{-1} metal at 0.3 V RHE),[18] PdSn (0.19 A mg^{-1} Pd at 0.2 V Ag/AgCl),[19] indicating Pd NS/G is an excellent electrocatalysts for direct formic acid fuel cells.

Fig.S13 XPS N1s spectra in Pd NP/GO and Pd NS/G samples, and Pd 3d spectra..

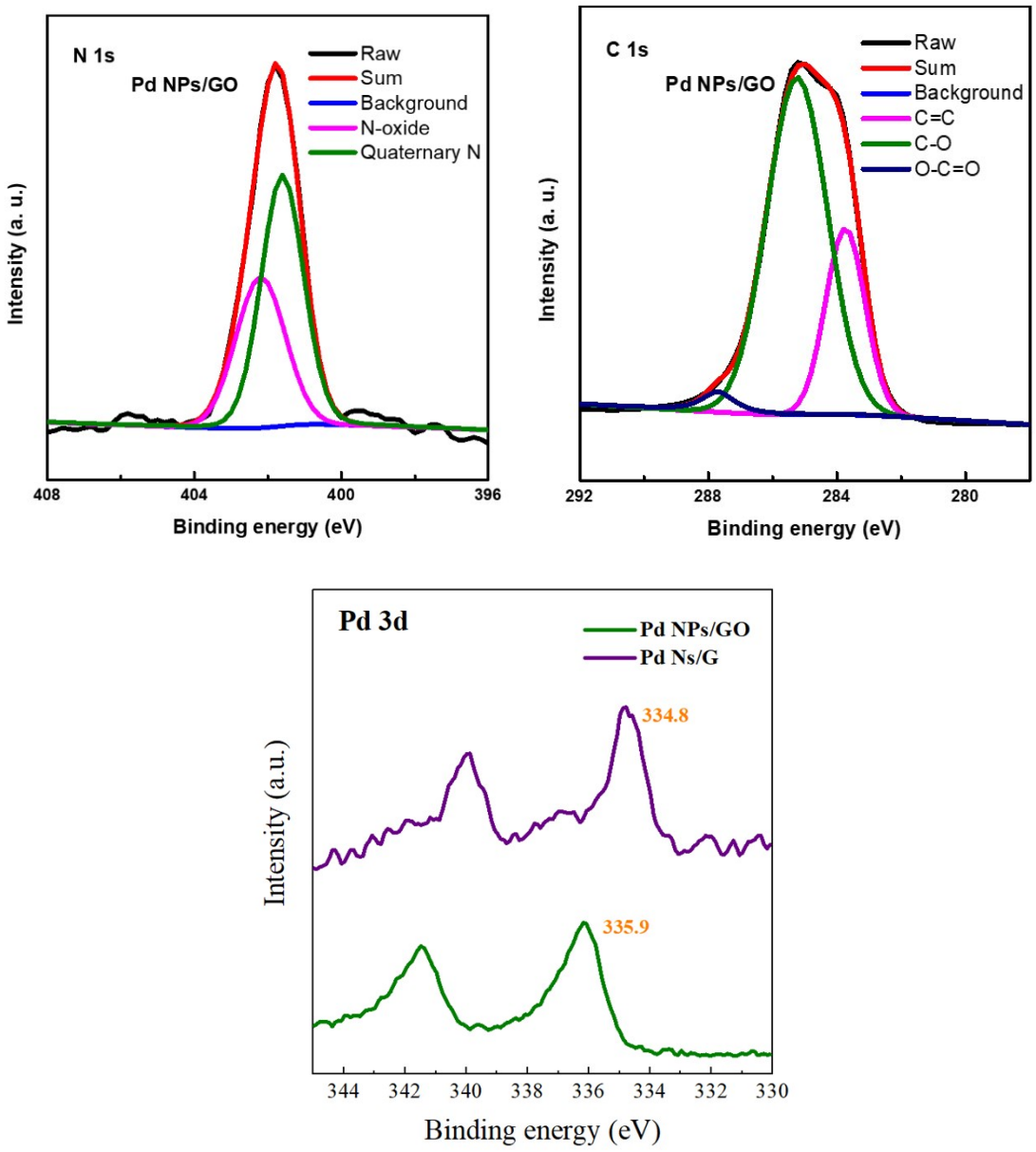

Table S1 Mass activities (peak current densities) of various metal catalysts for formic acid oxidation shown in Figure 4

Catalysts	Mass activities (A g^{-1})	Reference
PdCu multipods	0.15	20
PdCo	0.18	21
PdSn	0.19	22
Pd@NiBx	0.21	23
PdNi	0.22	24
PtBi	0.22	25
Pd sheets	0.30	26
PdAg/TiCrN	0.31	27
nano Pd	0.35	28
PdCu	0.38	24
PdNiCu	0.48	24
Pd@Au	0.52	29
PdNi nanowires	0.62	30
CNT-Pd	0.71	24
Pd3Pb	1.00	31
Pd-g-C3N4	1.02	32
Pd/WOx	1.15	20
Our Pd nanosheets	**1.16**	**this report**

Table S2 Chemical environments of C and N in Pd NPs/GO and Pd NS/G samples based on their deconvoluted XPS sub-peaks.

Samples	Pd NPs/GO	Pd NS/G
C=C	0.25	0.61
C-O	0.69	0.33
COOH	0.06	0.06
Quaternary Nitrogen	0.60	0.87
Nitrogen oxide	0.40	0.13

DFT Calculations

We carried out spin-polarized calculations within the density functional theory (DFT) framework as implemented in the Vienna *ab initio* simulation package (VASP).[1] The ion-electron interactions are represented by the projector-augmented wave (PAW) method[2] and the electron exchange-correlation by the generalized gradient approximation (GGA) with the Perdew-Burke-Ernzerhof (PBE) exchange-correlation functional.[3] The Kohn-Sham valence states were expanded in a plane-wave basis set with a cut-off energy of 400 eV. The Pd(4d5s), O(2s2p), C(2s2p) and H(1s) electrons were treated as valence states. The optimized lattice parameter of Pd bulk is 3.87 Å.

For Pd(111) and Pd(100), the models were a periodic slab with a (3×3) surface supercell contains four layers, in which the bottom two layers were frozen. For Pd(110), the models were a periodic slab with a (2×3) surface supercell contains eight layers, in which the bottom four layers were frozen. For Pd(211), the models were a periodic slab with a (1×3) surface supercell contains six layers, in which the bottom three layers were frozen. For Pd(311), the models were a periodic slab with a (2×3) surface supercell contains nine layers, in which the bottom four layers were frozen. The Brillouin-zone integrations were performed using a (7×7×1) Monkhorst-Pack mesh during the optimization. The iterative process considered was convergences, when the force on the atom was < 0.02 eV $Å^{-1}$ and the energy change was $<10^{-5}$ eV per atom.

Thermodynamic properties were estimated by means of in-house software Supy. The Gibbs free energies at 298.15 K and 1 atm were calculated with

$$G = H - TS = E_{DFT} + E_{ZPE} + \int_0^{298.15K} C_V dT - TS \qquad (1)$$

where E_{DFT} is the total energy obtained from DFT optimization, E_{ZPE} is the zero-point vibrational energy using the harmonic approximation,[4] C_V is the heat capacity, T is the kelvin temperature, and S is the entropy. The computational hydrogen electrode (CHE) model[5] was used to calculate the free energy of electro-catalytic OERs.

To build up the correlation between d-band center (DBC, ε_d) and coordination number (CN) of surface Pd atoms, we first calculated the generalized coordination number ($\bar{CN}$) of a surface Pd atom. $\bar{CN}$ is estimated arithmetically from the sum of the conventional coordination numbers (CN_j) of its n_i nearest neighbors and normalized by the maximum number of neighbors found in the bulk of the crystal (CN_{max})[6]

$$\bar{CN} = \sum_{j=1}^{n_i} \frac{CN_j}{CN_{max}} \qquad (2)$$

For FCC metal Pd bulk, the Pd atom has a maximum of 12 neighbors, and thus $CN_{max} = 12$.

Section 4: Theoretical calculations

Fig. S14. DFT-determined correlation between overpotentials of formic acid oxidation and d-band center of surface Pd atoms.

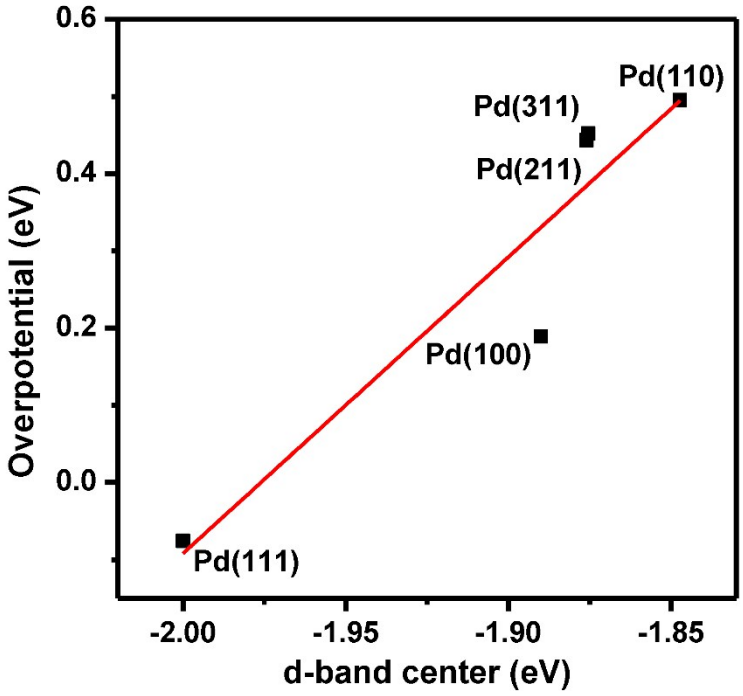

Table S3 DFT-determined generalized coordination number, d-band center and surface energy of various Pd facets, respectively.

Facets	**Pd(111)**	**Pd(100)**	**Pd(110)**	**Pd(211)**	**Pd(311)**
$\bar{CN}$	7.5	6.67	5.83	4.83	4.75
d-band center (eV)	-2	-1.89	-1.85	-1.87	-1.87
surface energy (eV/Å^2)	0.126	0.138	0.144	0.163	0.166

Table S4 Predicted Gibbs free energy profiles of formic acid oxidation over various Pd facets, respectively.

Species	E (eV)	TS (eV) 298.15K	ZPE (eV)	CvT (eV)	G (eV)
CO_2(g)	-23.02	0.66	0.31	0.058	-23.32
H_2(g)	-6.76	0.40	0.44	0.037	-6.69
HCOOH(l)	-29.81	0.44	0.89	0.079	-29.28
		Pd(111)			
*** + HCOOH(l)**	-195.97				-195.97
HCOOH*	-226.37	0.21	0.93	0.10	-225.54
HCOO*	-222.81	0.34	0.65	0.17	-222.33
CO_2*	-219.24	0.16	0.30	0.056	-219.04
*** + CO_2(g)**	-195.97				-195.97
		Pd(100)			
*** + HCOOH(l)**	-192.00				-192.00
HCOOH*	-222.43	0.21	0.93	0.10	-221.60
HCOO*	-218.97	0.33	0.62	0.16	-218.52
CO_2*	-215.21	0.097	0.30	0.034	-214.97
*** + CO_2(g)**	-192.00				-192.00
		Pd(110)			
*** + HCOOH(l)**	-262.51				-262.51
HCOOH*	-293.04	0.19	0.93	0.098	-292.21
HCOO*	-289.84	0.33	0.62	0.16	-289.38
CO_2*	-285.73	0.15	0.31	0.056	-285.52
*** + CO_2(g)**	-262.51				-262.51
		Pd(211)			
*** + HCOOH(l)**	-195.10				-195.10
HCOOH*	-225.57	0.26	0.94	0.12	-224.77
HCOO*	-222.34	0.31	0.63	0.18	-221.84
CO_2*	-218.33	0.012	0.30	0.009	-218.03
*** + CO_2(g)**	-195.10				-195.10
		Pd(311)			
*** + HCOOH(l)**	-294.52				-294.52
HCOOH*	-324.97	0.20	0.93	0.10	-324.14
HCOO*	-321.76	0.31	0.64	0.16	-321.27
CO_2*	-317.67	0.12	0.30	0.035	-317.46
*** + CO_2(g)**	-294.52				-294.52

References:

(1) Shao, Y. Y.; Wang, J.; Engelhard, M.; Wang, C. M.; Lin, Y. H. *J. Mater. Chem.* **2010**, *20*, 743-748.

(2) Zhang, S.; Shao, Y. Y.; Yin, G. P.; Lin, Y. H. *J. Mater. Chem.* **2009**, *19*, 7995-8001.

(3) Zhang, S.; Shao, Y. Y.; Yin, G. P.; Lin, Y. H. *Angew. Chem.-Int. Edit.* **2010**, *49*, 2211-2214.

(4) Nieminen, V.; Honkala, K.; Taskinen, A.; Murzin, D. Y. *J. Phys. Chem. C* **2008**, *112*, 6822-6831.

(5) Santos, E.; Quaino, P.; Soldano, G.; Schmickler, W. *Electrochem. Commun.* **2009**, *11*, 1764-1767.

(6) Hammer, B.; Norskov, J. K. In *Advances in Catalysis, Vol 45*; Academic Press Inc: San Diego, 2000; Vol. 45, p 71-129.

(7) Stamenkovic, V. R.; Fowler, B.; Mun, B. S.; Wang, G. F.; Ross, P. N.; Lucas, C. A.; Markovic, N. M.*Science* **2007**, *315*, 493-497.

(8) Arenz, M.; Stamenkovic, V.; Schmidt, T. J.; Wandelt, K.; Ross, P. N. Markovic, N. M. *Phys. Chem. Chem. Phys.* **2003**, *5*, 4242-4251.

(9) Babu, P. K.; Kim, H. S.; Chung, J. H.; Oldfield, E.; Wieckowski, A. *J. Phys. Chem. B* **2004**, *108*, 20228- 20232.

(10) Zhang, J.; Sasaki, K.; Sutter, E.; Adzic, R. R. *Science* **2007**, *315*, 220-222.

(11) Chen, Z. W.; Waje, M.; Li, W. Z.; Yan, Y. S. *Angew. Chem.-Int. Edit.* **2007**, *46*, 4060-4063.(12) Sun,S.H.;Jaouen,F.; Dodelet, J. P. *Adv. Mater.* **2008**, *20*, 3900-3904.

(13) Wang, J. J.; Chen, Y. G.; Liu, H.; Li, R. Y.; Sun, X. L. *Electrochem. Commun.* **2010**, *12*, 219-222.

(14) Huang, Y. J.; Zhou, X. C.; Liao, J. H.; Liu, C. P.; Lu, T. H.; Xing, W. *Electrochem. Commun.* **2008**, *10*, 621-624.

(15) Wang, J. J.; Yin, G. P.; Chen, Y. G.; Li, R. Y.; Sun, X. L. *Int. J. Hydrog. Energy* **2009**, *34*, 8270-8275.

(16) Zhang, S. X.; Qing, M.; Zhang, H.; Tian, Y. N. *Electrochem. Commun.* **2009**, *11*, 2249-2252.

(17) Morales-Acosta, D.; Ledesma-Garcia, J.; Godinez, L. A.; Rodriguez, H. G.; Alvarez-Contreras, L.; Arriaga, L. G. *J. Power Sources* **2010**, *195*, 461-465.

(18) Ji, X. L.; Lee, K. T.; Holden, R.; Zhang, L.; Zhang, J. J.; Botton, G. A.; Couillard, M.; Nazar, L. F. *Nat. Chem.* **2010**, *2*, 286-293.

(19) Zhang, Z. H.; Ge, J. J.; Ma, L. A.; Liao, J. H.; Lu, T. H.; Xing, W. *Fuel Cells* **2009**, *9*, 114-120.

(20) Chen, D.; Sun, P.; Liu, H.; Yang, J. Bimetallic Cu–Pd alloy multipods and their highly electrocatalytic performance for formic acid oxidation and oxygen reduction. J. Mater. Chem. A 2017, 5, 4421–4429.

(21) Mazumder, V.; Chi, M.; Mankin, M.; Liu, Y.; Metin, O.; Sun, D.; More, K.L.; Sun, S. A Facile Synthesis of MPd (M = Co, Cu) Nanoparticles and Their Catalysis for Formic Acid Oxidation. Nano Lett. 2012, 12, 1102–1106.

(22) Z. H. Zhang, J. J. Ge, L. A. Ma, J. H. Liao, T. H. Lu, W. Xing, Fuel Cells 2009, 9, 114-120.

(23) He, N.; Gong, Y.; Yang, Y. ScienceDirect an effective Pd@Ni-B/C anode catalyst for electro- oxidation of formic acid. Int. J. Hydrogen Energy 2018, 43, 3216–3222.

(24) Hu, S.Z.; Munoz, F.; Noborikawa, J.; Haan, J.; Scudiero, L.; Ha, S. Carbon Supported Pd-Based Bimetallic and

Trimetallic Catalyst for Formic Acid Electrochemical Oxidation. Appl. Catal. B 2016, 180, 758–765.

(25) X. L. Ji, K. T. Lee, R. Holden, L. Zhang, J. J. Zhang, G. A. Botton, M. Couillard, L. F. Nazar, Nat. Chem. 2010, 2, 286-293.

(26) Yin, X.; Chen, Q.; Tian, P.; Zhang, P.; Zhang, Z.; Voyles, P.M.;Wang, X. Ionic Layer Epitaxy of Nanometer-Thick Palladium Nanosheets with Enhanced Electrocatalytic Properties. Chem. Mater. 2018, 30, 3308

(27) Cui, Z.; Yang, M.; DiSalvo, F.J. Mesoporous Ti0.5Cr0.5N Supported PdAg Nanoalloy as Highly Active and Stable Catalysts for the Electro-Oxidation of Formic Acid and Methanol. ACS Nano 2014, 8, 6106–6113.

(28) Xi, Z.; Erdosy, D.P.; Mendoza-Garcia, A.; Duchesne, P.N.; Li, J.; Muzzio, M.; Li, Q.; Zhang, P.; Sun, S. Pd Nanoparticles Coupled to WO2.72 Nanorods for Enhanced Electrochemical Oxidation of Formic Acid. Nano Lett. 2017, 17, 2727–2731.

(29) Zhou, W.J.; Lee, J.Y. Highly active core–shell Au@Pd catalyst for formic acid electrooxidation. Electrochem. Commun. 2007, 9, 1725–1729.

(30) Du, C.Y.; Chen, M.; Wang, W.G.; Yin, G.P. Nanoporous PdNi Alloy Nanowires as Highly Active Catalysts for the Electro-Oxidation of Formic Acid. ACS Appl. Mater. Interfaces 2011, 3, 105–109.

(31) Gunji, T.; Noh, S.H.; Tanabe, T.; Han, B.; Nien, C.Y.; Ohsaka, T.; Matsumoto, F. Enhanced Electrocatalytic Activity of Carbon-Supported Ordered Intermetallic Palladium–Lead (Pd3Pb) Nanoparticles toward Electrooxidation of Formic Acid. Chem. Mater. 2017, 29, 2906–2913.

(32) Zhang, W.; Huang, H.; Li, F.; Deng, K.; Wang, X. Palladium nanoparticles supported on graphitic carbon nitride-modified reduced graphene oxide as highly efficient cat alysts for formic acid and methanol electrooxidation. J. Mater. Chem. A 2014, 2, 19084–19094.

(33) G. Kresse, J. Hafner, Physical Review B 1994, 49, 14251.

(34) P. E. Blöchl, Physical Review B 1994, 50, 17953.

(35) J. P. Perdew, K. Burke, M. Ernzerhof, Physical review letters 1996, 77, 3865.

(36) V. Barone, The Journal of chemical physics 2004, 120, 3059-3065.

(37) J. K. Nørskov, J. Rossmeisl, A. Logadottir, L. Lindqvist, J. R. Kitchin, T. Bligaard, H. Jonsson, The Journal of Physical Chemistry B 2004, 108, 17886-17892.

(38) X. Tian, X. Zhao, Y.-Q. Su, L. Wang, H. Wang, D. Dang, B. Chi, H. Liu, E. J. Hensen, X. W. D. Lou, Science 2019, 366, 850-856.